HHS Public Access

Author manuscript

Nat Biomed Eng. Author manuscript; available in PMC 2026 March 18.

Published in final edited form as:

Nat Biomed Eng. 2025 September ; 9(9): 1517–1530. doi:10.1038/s41551-025-01389-6.

A biochemical sensor with continuous extended stability in vivo

Yihang Chen[1,2,8], **Kaiyu X. Fu**[2,3,4,8], **Renee Cotton**[5], **Zihao Ou**[1], **Jean Won Kwak**[2], **Jun-Chau Chien**[2,3], **Vladimir Kesler**[2,3], **Hnin Yin Yin Nyein**[2,3], **Michael Eisenstein**[2,3], **H. Tom Soh**[2,3,6,7,✉]

[1]Department of Materials Science and Engineering, Stanford University, Stanford, CA, USA.

[2]Department of Radiology, Stanford University, Stanford, CA, USA.

[3]Department of Electrical Engineering, Stanford University, Stanford, CA, USA.

[4]Department of Chemistry and Biochemistry, University of Notre Dame, Notre Dame, IN, USA.

[5]Department of Comparative Medicine, Stanford University, Stanford, CA, USA.

[6]Department of Bioengineering, Stanford University, Stanford, CA, USA.

[7]Chan Zuckerberg Biohub, San Francisco, CA, USA.

[8]These authors contributed equally: Yihang Chen, Kaiyu X. Fu.

Abstract

The development of biosensors that can detect specific analytes continuously, in vivo, in real time has proven difficult due to biofouling, probe degradation and signal drift that often occur in vivo. By drawing inspiration from intestinal mucosa that can protect host cell receptors in the presence of the gut microbiome, we develop a synthetic biosensor that can continuously detect specific target molecules in vivo. The biomimetic multicomponent sensor features the hierarchical nano-bio interface design with three-dimensional bicontinuous nanoporous structure, polymer coating and aptamer switches, balancing small-molecule sensing and surface protection in complex biological environments. Our system is stable for at least 1 month in undiluted serum in vitro or 1 week implanted within the blood vessels of free-moving rats, retaining over 50% baseline signal and reproducible calibration curves. We demonstrate that the implanted system can intravenously track pharmacokinetics in real time even after 4 days of continuous exposure

Reprints and permissions information is available at www.nature.com/reprints.

✉**Correspondence and requests for materials** should be addressed to H. Tom Soh. tsoh@stanford.edu.

Author contributions

Y.C. and K.X.F. conceived the project. H.T.S. supervised the project. Y.C. and K.X.F. initiated the idea of using a hierarchical nanoarchitecture for long-term stable biosensing in complex biological matrices. Y.C., K.X.F. and H.T.S. designed the experiments. Y.C. performed the experiments, and collected and analysed the data. Y.C. and Z.O. conducted the optical experiments and image analysis. R.C. performed animal surgeries and trained Y.C. Y.C., J.W.K and J.-C.C. worked on improving intravenous microwire probes. V.K. and H.Y.Y.N. advised on electrochemical sensing. Y.C., K.X.F., M.E and H.T.S. co-wrote the paper. All authors discussed the results and commented on the paper.

Competing interests

Y.C., K.X.F. and H.T.S. are listed as co-inventors on a patent application related to this work filed at the US Patent and Trademark Office (No. PCT/US2024/060103). All other authors declare no competing interests.

Reporting summary

Further information on research design is available in the Nature Portfolio Reporting Summary linked to this article.

to flowing blood within rat femoral vein. In this way, our work provides a generalizable design foundation for biosensors that can continuously operate in vivo for extended durations.

Blood tests are a cornerstone of clinical care and health monitoring, but the vast majority of blood tests are only designed to provide instantaneous measurements at a single point in time[1]. Compact or wearable sensors that enable continuous measurement of circulating analytes could greatly extend the use of blood-based monitoring by tracking disease states, drug dosing, or metabolic and physiological activity in a wide range of clinical and non-clinical settings[2–6]. Numerous studies have demonstrated that aptamer-based electrochemical biosensors can provide a generalizable molecular detection framework that achieves good sensitivity and specificity for relatively short-term continuous in vitro and in vivo measurements of a variety of small-molecule analytes[4,7–13]. In this design, analyte binding induces a conformational change in a redox-tagged aptamer strand[14]; this in turn alters the electron transfer rate of the redox tag to the electrode surface, producing a measurable change in current. The subsequent dissociation of the target then allows the aptamer switch to ‘reset’, restoring baseline current and offering the potential for continuous real-time detection[15,16]. Electrochemical aptamer-based sensor platforms can deliver a sensitive, rapid and highly specific response to changes in analyte concentration. However, none of the systems described so far has been demonstrated for extended use in the complex and challenging environment of the bloodstream, and the longest duration demonstrated for such an in vivo sensor so far is less than half a day[16], which is insufficient for many applications in clinical or personal health monitoring. For these reasons, many biosensor development efforts have focused on less challenging sample matrices such as tears, saliva, sweat and interstitial fluid[17].

Many challenges have confounded past attempts at long-term in vivo detection in the bloodstream[18–20]. First, any blood-interfacing system must be capable of resisting surface fouling by proteins, cells and other biomolecules in the sample matrix[21]. Such fouling already limits the length of time that systems for routine medical procedures, such as dialysis and cardiopulmonary bypass, can be used to just a few hours[22]. In addition, most biochemical sensors rely on antibodies, enzymes or aptamers that are vulnerable to chemical and enzymatic degradation, as well as non-specific binding to interferents[18,23]. Several strategies have been developed to overcome these challenges, including the use of passive filtration systems[15] or additive coatings[16,24,25] that protect the sensor and its associated bioreceptors from fouling and degradation. For example, our group has leveraged a microfluidic system with two stacked laminar flows to dynamically filter out blood cells and other high-molecular-weight interferents in flowing blood before aptamer-based sensing[15]. Unfortunately, this approach suffers from measurement time lag due to blood passing through the device as well as mechanical vulnerability in terms of maintaining laminar flow conditions. One can also employ surface modification with antifouling self-assembled monolayers (SAMs)[26,27], but gradual monolayer desorption due to thermal, electrical or fouling effects erodes the effectiveness of such measures, ultimately leading to device failure. Nanostructured biosensors have also exhibited the potential to suppress non-specific protein binding by limiting plasma protein access to the sensor surface[28], and our group has demonstrated that nanoporous electrode designs can protect immobilized aptamers

against mechanical shearing during implantation[29]. Nevertheless, complex interactions with the surrounding biological milieu have generally limited the operational duration of such electrodes to less than 12 h in vivo[29]. As such, there is still no reliable and generalizable framework for achieving stable and accurate biomolecular detection of a broad range of analytes in vivo over extended periods of time.

Despite these challenges, innate biochemical sensing mechanisms in living organisms retain the capacity for monitoring biochemical and immunoregulatory signals in highly complex physiological environments over the lifetime of the organism[30]. One common strategy for preserving the function of endogenous molecular receptors involves establishing a physically restricted zone for protecting molecular recognition elements against fouling or damage by interferents[31,32]. For example, the intestinal mucosa has evolved to form a hierarchically layered interface consisting of protruding microvilli adorned with target-binding molecular switches such as Toll-like receptors (TLRs)[33], which are in turn insulated against the gut interior by a hyperbranched glycocalyx coating[30,34,35]. The resulting nanostructure serves as a physical barrier that segregates the host tissue from trillions of commensal—but also potentially immunogenic—gut microbes while still granting essential metabolic and immune receptors ready access to biologically important protein and small-molecule ligands[30].

In this work, we describe a biomimetic multicomponent sensor design that enables continuous analyte detection in the bloodstream, drawing inspiration from the structural and functional configuration of the mammalian intestinal mucosa. Our Stable Electrochemical Nanostructured Sensor for Blood In situ Tracking (SENSBIT) system balances the capacity for sensitive small-molecule monitoring and robust antifouling performance in vitro and in vivo, retaining excellent sensitivity and stability for detecting the antibiotic kanamycin even after protracted exposure to blood. SENSBIT features a three-dimensional (3D) nanoporous gold surface that emulates the complex structure of epithelial microvilli, sequestering electrochemically modified aptamer switch ‘receptors’ from interferents in the sample matrix. An additional coating of hyperbranched polymer molecules on the porous gold surface mimics the additional protection conferred by mucosal glycans, insulating the sensor against degradation and fouling. When challenged with undiluted serum in vitro, we show that SENSBIT can maintain a stable baseline and consistent sensitivity for one month. We subsequently performed long-term intravenous implantation of our sensor into free-moving rats and showed that SENSBIT maintains >60% chronic baseline stability and robust sensitivity for kanamycin detection after 7 days, far longer than any other published in vivo sensor described so far. Finally, we implanted SENSBIT in rat femoral veins and achieved real-time pharmacokinetic monitoring of kanamycin in the bloodstream over the course of 4 days with no need for signal correction. SENSBIT’s resilience and stability even after prolonged exposure to flowing blood and living tissue opens an exciting avenue for the development of biosensors that retain robust performance in vivo for extended periods of time.

Results and discussion

The design concept for the mucosa-inspired SENSBIT system

SENSBIT integrates multiple technological advances to overcome the challenges that have previously prevented the development of blood-interfacing biosensors for long-term in vivo molecular monitoring. We have modelled our system on insights from a naturally occurring system for sensing in complex biological matrices: the intestinal mucosal interface. This interface plays two crucial roles, acting as a mechanical and physicochemical barrier against shear-induced damage and harmful molecules, while also serving as a frontline sensor for the real-time acquisition of bacteria-derived immunomodulatory signals[30]. These dual functions are enabled by the hierarchical structure of the mucosal interface, which consists of protruding microvilli that feature a hyperbranched glycocalyx coating as well as target-binding molecular switches such as TLRs (Fig. 1a)[30,34,35]. The glycocalyx coating forms an intermeshed network that acts as a spatial filter that insulates and protects the underlying epithelium against most biomolecules while still allowing important pathogen-derived signals such as unmethylated CpG-containing DNA sequences to pass through and engage with relevant receptors on the microvillar surface[31]. SENSBIT imitates this natural interface at multiple levels (Fig. 1b). The sensor surface itself consists of a 3D bicontinuous nanoporous gold (npAu) surface, analogous to the high-surface-area structure of the microvilli, which is coated with electrochemically modified aptamer switch receptors as well as a hyperbranched polyethylene glycol (PEG) coating that mimics the meshed glycocalyx coating of the mucosa. SENSBIT's redox-tagged aptamer switches undergo reversible binding-induced molecular switching to generate a measurable electrochemical readout in the presence of their target analyte. Target concentration can be calculated from the signal gain of the electrochemical signals, which can be quantified with the redox-tag current peaks from square-wave voltammetry (SWV), enabling real-time molecular quantitation[15].

Our priority for SENSBIT was to enable long-term in vivo analyte monitoring in complex biological environments such as undiluted plasma and whole blood without sacrificing performance to signal degradation or excess background. As proof of concept, we developed a SENSBIT system that tracks changing concentrations of the small-molecule antibiotic kanamycin. This is a clinically relevant example, as kanamycin-based therapy to treat serious bacterial infections usually lasts weeks, and the dose could theoretically be tuned and optimized in real time on the basis of data from a continuous sensor[37]. In addition, there is an existing electrochemical aptamer switch that has been used to sensitively and specifically report concentrations of this analyte in other sensor systems, binding to kanamycin with an equilibrium dissociation constant (K_D) of ~0.5 mM[38].

Assembling and optimizing the SENSBIT device

We constructed our sensors in a stepwise fashion (Supplementary Fig. 1). The bicontinuous npAu surface was custom designed to achieve an apical pore size of ~17.08 ± 4.28 nm (Supplementary Fig. 2), which was accessible for subsequent modification with 26-nucleotide kanamycin aptamer switches (<10 nm in length) via thiol–gold interactions. These aptamers were modified with a methylene blue (MB) functional group at their 3'

terminus, and this moiety acts as the redox reporter for detecting target-binding events. The aptamer-loaded nanoporous gold surface was subsequently modified with a PEG-based polymer coating. Finally, we fully passivated the electrode surface with 6-mercapto-1-hexanol (MCH) backfill, which coats the spaces remaining between the polymer molecules and aptamer switches to suppress non-specific redox reactions with the electrode surface. Details of this assembly process are provided in the Methods section.

We performed an experiment to identify optimal polymer candidates for the SENSBIT coating layer, assessing PEG coatings with different molecular weights and structures. The PEG polymer candidate pool (M_W: 2,000–20,000 Da, linear or hyperbranched) was narrowed down according to the calculated polymer brush sizes in physiological conditions[39,40] (Supplementary Note 1). We employed a nuclease-based assay to rapidly quantify the extent to which different coatings minimize the extent of protein interactions with aptamer switches on the SENSBIT surface (Supplementary Fig. 3)[41]. We selected S1 nuclease for three reasons. First, the ubiquity of endogenous nucleases in biofluids means that any DNA- or RNA-based biosensor will require robust nuclease resistance for long-term use[42]. Second, S1 nuclease is an endonuclease that specifically degrades single-stranded nucleic acids; as such, S1 nuclease activity will result in the loss of MB redox reporter moieties, leading to a measurable loss of electrochemical signal[41]. Finally, the hydrodynamic size of S1 nuclease is comparable to or smaller than most serum proteins, and thus offers a robust test of the size-exclusion mechanism of our mucosa-inspired nanostructures[43]. We subjected SENSBIT systems modified with the PEG polymer candidates to S1 nuclease concentrations of 60 U ml^{-1}, which is more than an order of magnitude higher than physiological levels, to accelerate the identification of optimal polymer coating.

We characterized the extent of degradation in real time by electrochemically measuring signal loss over time (Fig. 1c). For purposes of comparison, we also tested a PEG-free, aptamer-modified npAu electrode, as well as an aptamer-modified planar gold electrode (pAu) with the same range of coatings. The signal gain in these and subsequent experiments was defined as the ratio of SWV peak current at a defined concentration relative to the target-free baseline (Supplementary Note 2). After a 30-min nuclease challenge, the PEG-free pAu electrode experienced a sharp reduction in signal by 85.6%, essentially rendering the sensor unusable. In comparison, PEG-free npAu or hyperbranched PEG-coated pAu electrodes achieved considerably reduced degradation, with 45.4% and 39.6% signal loss, respectively (Fig. 1c and Supplementary Fig. 3c). The combination of npAu and linear PEG (M_W = 2,000 Da) yielded significantly better synergistic protection against electrochemical decay, with signal loss of just 9.8% after 30 min. When we replaced the simple linear PEG coating with hyperbranched PEG (8-arm, M_W = 20,000 Da), we observed even greater suppression of electrochemical decay, with negligible SWV signal change (1.92 ± 0.46%) after 30 min. We also confirmed the superior suppression of nuclease-induced electrochemical signal decay in the hyperbranched PEG-coated npAu electrodes with another nuclease challenge experiment using DNase I, which is typically present in human blood samples (Supplementary Fig. 4). These results collectively indicate that this hierarchical sensor configuration, in which molecular switches are coupled with protruding nanostructures and a hyperbranched polymer coating, can effectively shield aptamer

switches from proteins in the sample. We further studied the mechanisms underlying this combinational protection by tuning the polymer size (Supplementary Fig. 3c), polymer coating condition, polymer choice (Supplementary Fig. 5) and pore size (Supplementary Fig. 6). On the basis of these results, we concluded that SENSBIT's protein resistance is optimal with the combination of nanoporous gold with hyperbranched PEG (PEG 8-arm, M_W = 20,000 Da). We subsequently compared the protein resistance of SENSBIT to other previously published strategies for aptamer sensor protection (Supplementary Table 1), using the same nuclease assay described above. Our results showed that all physical shielding, self-assembled monolayer (SAM) engineering and nanostructured electrode methods impeded nuclease-mediated sensor degradation better than pAu/MCH, but none matched the robust stability of SENSBIT (Fig. 1d and Supplementary Fig. 7).

The hydrodynamically dense nanostructures formed by the hyperbranched PEG layer raised potential concerns about whether target analytes have sufficient access to the aptamer switches immobilized within the nanostructure, and whether those captured biomolecules can subsequently exit the nanostructure and re-enter the bulk biofluid[44]. We therefore evaluated the short-term sensitivity and reversibility of SENSBIT in a series of in vitro experiments with undiluted human serum. To assess sensitivity, we quantified the SWV signal gain produced by SENSBIT and pAu-based kanamycin sensors with and without a PEG 8-arm protective layer in undiluted human serum ~2 min after spiking in kanamycin to a final concentration of 10 mM (Supplementary Fig. 8a). Introducing a PEG coating onto the pAu surface undermined sensor sensitivity, resulting in a 17.59% lower signal gain relative to a PEG-free pAu electrode (signal gain = 48.65 ± 3.99%). This confirmed the potential for additional steric hindrance that could affect target access to aptamer switches. However, the use of the npAu electrode with a hyperbranched PEG coating mitigated these deleterious effects, yielding a vastly superior signal gain relative to the pAu system (81.18 ± 1.45%). This enhancement can be explained by curvature-mediated steric effects on aptamer switch conformational change[45] (Supplementary Fig. 9) and the accelerated electron transfer that occurs within nanostructured electrodes, a phenomenon that has been discussed in detail in our previous work[46]. We then characterized reversibility by quantifying the extent to which the SWV signal returned to baseline after being challenged with 10 mM kanamycin in undiluted human serum and subsequently washing with kanamycin-free serum from the same batch (Supplementary Fig. 8b). The regenerated signals measured 2 min after washout revealed that SENSBIT enhanced reversibility and enabled the sensor to reset to near-baseline after washout with kanamycin-free serum. In contrast, the unprotected PEG-free pAu control experienced considerable signal drift, potentially due to non-specific binding of serum proteins to the electrode surface, which in turn hindered the aptamers' capacity to undergo target-binding-induced conformational change. Real-time measurements of kanamycin dose-in and washout in undiluted human serum exhibited no hysteresis, and similar on/off response times for SENSBIT in kanamycin sensing and regeneration compared to pAu sensors over the course of 50 min (Supplementary Fig. 10). Kinetically, SENSBIT showed no delay compared with a pAu control in reading out kanamycin spike-in and washout, with a temporal resolution of 4 s (Supplementary Fig. 11 and Note 3). We thus conclude that the SENSBIT architecture can maintain kanamycin transport across its nanostructures without compromising sensor performance in terms of sensitivity,

reversibility or temporal resolution. We also determined that the same SENSBIT architecture can be generalized to sense other small-molecule analytes (Supplementary Fig. 12). For example, we have shown that the chemotherapy drug doxorubicin (DOX) and ATP can both be sensed with SENSBIT by simply incorporating the appropriate aptamer switches[29,47] (Supplementary Fig. 13). However, we also observed evidence for an upper bound to the size of analytes that can be measured with SENSBIT. Our SENSBIT sensor for vancomycin (M_W ~1.5 kDa) was largely unresponsive relative to its pAu counterpart (Supplementary Fig. 12), most probably due to the same exclusion mechanism that prevents interferents from damaging the aptamer probes or fouling the sensor surface. Together, these results indicate that this design is successful at preventing sensor contamination while still allowing small molecular target molecules to engage with aptamer switches on the electrode surface.

Month-long stable operation of SENSBIT in human serum

To evaluate the long-term stability of our sensors during extended exposure to complex biological matrices, we characterized the baseline response and sensitivity of unprotected sensors and the optimized SENSBIT system over the course of a month-long incubation in undiluted human serum (Supplementary Note 2). We quantified baseline stability in terms of signal deterioration over time in the absence of kanamycin, with SWV measurements collected on days 1, 3, 7, 14 and 28 and quantified relative to the sensors' initial SWV peak current at day 0. The baseline signal from the pAu electrode fell by >50% within 7 days, with drifting current readings and unstable voltammograms indicating considerable degradation of the sensor[27] (Fig. 2a). In contrast, SENSBIT yielded reproducible voltammograms (Fig. 2b), maintaining 90.27 ± 1.46% of its original baseline signal after 1 week, and more surprisingly, >70% baseline signal after 28 days of continuous exposure to undiluted human serum (Fig. 2c).

We next assessed long-term kanamycin sensitivity by generating calibration curves on the basis of signal gain from various concentrations of kanamycin at days 1, 3, 7, 14 and 28 of continuous exposure to undiluted human serum. The calibration curves were obtained by spiking fixed amounts of kanamycin up to a final concentration of 10 mM while collecting measurements throughout. At the end of each measurement, we washed out the kanamycin and replaced the sample with fresh undiluted human serum with no kanamycin. For the pAu control sensor, we observed considerable loss of sensitivity over time, with significantly reduced signal gain apparent by day 1 (Fig. 2d). This indicates that aptamer-target binding was probably impaired either by non-specific binding of the sensor to plasma proteins or by degeneration of the aptamer switches. In contrast, SENSBIT exhibited minimal calibration curve drift over the course of a month in human serum (Fig. 2e), with reproducible signal gain observed at each target concentration. We fitted our signal gain data to the Langmuir isotherm model, which assumes one target-binding site per aptamer switch[48]:

$$\text{Signal gain} = \frac{B_{\max} \times [\text{analyte}]}{K_D + [\text{analyte}]} \times 100\% \quad (1)$$

where B_{max} is the fitting maximum signal gain of the sensor. The calibration curves of both the pAu control sensor and SENSBIT exhibited good fit to the model, with $R^2 > 0.90$ at day 0. SENSBIT maintained this good fit after 1 month of human serum exposure, with $R^2 > 0.95$, while pAu exhibited poor target-signal gain correlation after 2 weeks, with R^2 of 0.083 (Supplementary Fig. 14). The SENSBIT sensors generally experienced negligible drift after a month-long human serum challenge, whereas the B_{max} of the unprotected pAu sensor decreased dramatically over time (Fig. 2f). These results indicate that the SENSBIT design effectively protects the sensor against fouling and degradation while enabling stable biochemical sensing operation for up to a month in undiluted serum.

SENSBIT integrity after incubation with plasma or blood

Sensing in whole blood introduces several additional challenges in comparison with serum. For example, despite advances in biomaterials, fouling on blood-interfacing devices remains a common problem, and intravenous devices often fail within a few hours after implantation due to extensive blood cell and clot deposition on the device surface[22]. This contamination is initially activated by protein adsorption, where fibrinogen is typically the first plasma protein adhering to blood-interfacing devices, followed by platelet, leucocyte and red blood cell adhesion and eventual material-induced thrombosis[21,49,50]. For an electrochemical aptamer-based sensor, such non-specific fouling obstructs aptamer-target binding and sterically impedes the conformational change required for signal readout[23]. We therefore investigated the blood cell coverage density on devices with different surface treatments after overnight (14 h) incubation with human whole blood. Microscopic analysis revealed fewer blood cells adhering to our SENSBIT surface compared with the pAu control (Fig. 3a). Even without PEG coating, the npAu electrode showed only 2.83 ± 0.98% blood cell coverage relative to 28.47 ± 3.93% for the pAu surface (Fig. 3b). The full SENSBIT design further suppressed blood cell adhesions to just 1.29 ± 0.27% surface coverage.

In principle, even low levels of blood cell fouling might still block analyte access to the sensor and undermine sensor sensitivity. We therefore performed in situ sectioning and visualization of the interface between single blood cells and the SENSBIT surface using focused ion beam scanning electron microscopy (FIB-SEM; Fig. 3c). This cross-section revealed that blood cell coverage on SENSBIT only blocks limited regions of the apical surface, and that the complex porous structure of the SENSBIT electrodes should still support lateral target transport even if direct access from the apical surface is blocked (Fig. 3c, magnified view). We also assessed the potential for protein-induced blockage within the 3D structure of SENSBIT by characterizing the electrode interface after exposure to chicken plasma for 19 days in vitro. We chose plasma rather than blood to eliminate potential interference from whole blood cells, and pre-filtered the chicken plasma through a 0.2-μm filter to prevent protein aggregation and sedimentation before interaction with the electrode surface. Finally, we imaged the protein-fouled interface after washout. As expected, plasma protein fouled the SENSBIT apical surface and formed protein islands on top that could readily be visualized from 52° tilted SEM (Fig. 3d). Interestingly, by locally FIB milling the fouled apical surface and in situ sectioning the protein-fouled SENSBIT surface regions, we determined that the internal porous infrastructure SENSBIT electrode remained unobstructed, with minimal fouling observed within (Fig. 3d, magnified view;

Supplementary Fig. 15). We therefore concluded that small-molecule analytes can still freely access aptamers immobilized within the SENSBIT electrode via the bicontinuous 3D tunnels and neighbouring openings, even for regions where the apical electrode surface is covered by a fouling ‘island’. This is in keeping with the robust sensitivity that we observed with SENSBIT even after a month-long assessment in human serum (Fig. 2e). To further investigate whether npAu alone could provide the achieved fouling resistance, we characterized PEG-free npAu and SENSBIT surfaces after a week-long incubation in human whole blood. The uncoated npAu apical surface was severely fouled, with cellular contents and blood protein aggregates directly obstructing and infiltrating into the nanopores, whereas SENSBIT was only blocked at a few sites at the apical surface, with limited obstruction of the porous nanostructures (Supplementary Fig. 16). The inadequate protein resistance of uncoated npAu can also be demonstrated on the basis of apparent signal loss after challenge with nucleases (Fig. 1c). We thus conclude that SENSBIT’s hierarchical architecture of nanoporous electrode and hyperbranched polymer coating is necessary for long-term stability in complex biological environments.

Finally, we assessed the extent to which SENSBIT is protected against protein–surface interactions that arise during material-induced thrombosis. In this state, fibrinogen anchors onto materials and subsequently serves as the backbone for further protein adsorption and thrombosis within minutes of surface contact[21]. This could sterically affect the conformational change of aptamers for electrochemical reporting and hinder target transport within the sensor[23]. To test this, we incubated PEG-free and PEG-coated pAu and npAu sensors with human whole blood containing fluorescently labelled fibrinogen (150 μg ml^{-1}) for 2 h at 37 °C. We then washed the sensors and imaged the electrodes with an epifluorescence microscope. Fibrinogen coverage was greatly reduced on the SENSBIT surface compared with PEG-free pAu (Fig. 3e). The use of either PEG-free npAu electrodes or PEG-coated pAu electrodes partially reduced fibrinogen coverage, but the bioinspired hierarchical configuration with npAu and hyperbranched PEG coating in the SENSBIT design reduced fibrinogen adhesion to just 0.27 ± 0.18% versus 8.53 ± 5.52% for PEG-free pAu (Fig. 3f). We therefore conclude that SENSBIT can effectively mitigate the impact of cellular and protein interferents in whole blood.

Correction-free continuous intravenous monitoring

We next characterized SENSBIT’s intravenous real-time continuous monitoring performance over the course of several hours in anaesthetized rats. For these experiments, we prepared an implantable microwire probe with SENSBIT (or pAu as a control) bundled with an Ag/AgCl reference electrode and a Pt counter electrode (Fig. 4a). We used the reference or counter electrodes as prepared, with no additional treatment[51] (Supplementary Note 4). During the surgical procedure, the probes were directly implanted and fed into rat femoral veins with minimal tissue damage. The implanted probes were secured onto the femoral vein by tissue glue and surgical sutures at the connection ends. Successful intravenous access was confirmed on the basis of blood flow after retracting the implanted probes (Supplementary Video 1). The I/O port of the probe was connected to an external potentiostat for real-time SWV data extraction and analysis with customized codes, while the three electrodes were fully exposed to the blood within the femoral veins. Considering

the in vivo data quality, we then continuously read out the raw electrochemical SWV signals without administering kanamycin. Following the collection of the raw electrochemical signal, we performed target estimation by using a pre-calibrated inverse-Langmuir standard curve to back-calculate target concentrations on the basis of the electrochemical signal gain[16,48]:

$$\text{signal gain } (t) = \left(\frac{\text{sensor readout } (t)}{\text{sensor baseline}} - 1 \right) \times 100\% \tag{2}$$

$$[\text{analyte}]_{\text{Estimated}} = \frac{K_D}{\frac{B_{max}}{\text{signal gain}(t)} - 1} \tag{3}$$

SENSBIT experienced minimal baseline signal drift during 2.5 h of continuous monitoring, with no need for drift-correction algorithms, while pAu probes experienced progressive signal degradation with ~30% signal loss by the end of the experiment (Supplementary Fig. 17). We next characterized SENSBIT's capacity for intravenous monitoring of real-time changes in kanamycin pharmacokinetics. After 10–40 min of stable baseline visualization, we administered kanamycin via retro-orbital sinus injection (400 mg kg^{-1}). Conventional pAu probes without PEG coating exhibited negligible target-induced signal change, with degrading SWV signal over time, rendering them ill-suited for continuous monitoring over several hours (Fig. 4b). In contrast, SENSBIT probes delivered robust biosensing performance: the real-time SWV signal initially increased and reached a peak ~36 min after injection due to redistribution in flowing blood, after which the signal gradually decayed due to elimination and metabolism over the following 3 h (Fig. 4c and Supplementary Fig. 18). To estimate kanamycin concentrations from these measurements, we generated calibration curves in vitro at room temperature before and after implantation, and in parallel, we also confirmed that the binding affinity of our aptamer-based sensors was not meaningfully different at room temperature versus body temperature (Supplementary Fig. 19). These results confirmed that there was minimal decay in the sensitivity of our implanted biosensors, with reproducible signal gain observed at each target concentration (Supplementary Fig. 20). This allowed us to eliminate the need for post-calibration and correction algorithms to compensate for baseline and sensitivity drift during hour-long blood interface, enabling real-time calculation of intravenous kanamycin concentrations at each timepoint from the raw SWV signals with the pre-calibrated SENSBIT probes.

Multiday SENSBIT stability in freely moving rats

We systematically characterized the stability of the baseline response and sensitivity of SENSBIT after an extended duration of intravenous implantation in free-moving rats. Given the difficulty of distinguishing target-induced signal gain from the effects of drift during in vivo experiments, we assessed SENSBIT's stability by performing sensor calibration in phosphate-buffered saline (PBS) containing defined concentrations of kanamycin both

before and after various durations of intravenous implantation (Fig. 5a). Implantation was performed as described above, and after implantation and recovery, the rats were able to move freely while the implanted electrode probes were constantly subjected to blood flow and mechanical strain (Supplementary Video 2). The implanted pAu and SENSBIT sensors did not compromise blood cell viability or proliferation and exhibited good biocompatibility during 1-week intravenous implantation (Supplementary Fig. 21).

To begin, we quantified the baseline stability of the sensors by comparing sensor performance in kanamycin-free PBS buffer with external reference and counter electrodes before and after 2 days of implantation. The retracted SENSBIT sensor surface has no obvious fouling (Supplementary Fig. 22). Functionally, the pAu sensor lost its baseline after implantation, with indiscernible SWV peaks (Fig. 5b), while SENSBIT maintained comparable SWV peak levels post implantation (Fig. 5c). Next, we examined how baseline stability was affected by both surgical implantation and protracted sensor interface with the intravenous environment (Supplementary Note 2). The former is associated with acute mechanical damage to the probe during implantation as well as fast-activation processes in the blood (for example, rapid adsorption of plasma proteins and adhesion of non-activated platelets)[50], whereas the latter involves progressive contributions of factors such as continuous blood shearing, nuclease degradation and gradual deposition of proteins and cells onto the probe surface. Surgical baseline stability was quantified as the ratio of the baseline SWV signal in buffer after 20 min of intravenous implantation to the baseline pre-implantation SWV signal of the same probe in buffer. SENSBIT probes exhibited superior surgical baseline stability of 82.58 ± 13.16% (Supplementary Fig. 23), whereas the pAu probes retained just 14.99 ± 13.75% of their baseline signal level post surgery. The longer-term baseline stability was quantified as the ratio of the extracted baseline SWV peak signal in buffer after multiple days of intravenous implantation in free-moving rats relative to the baseline obtained before implantation. This value was then normalized by dividing by the ratio that we calculated for the surgical baseline stability, which we defined as the chronic baseline stability (Supplementary Note 2). This allowed us to quantify the progressive intravenous effects that reduce biosensor performance over a multiday interface with the circulation. As expected, pAu probes underwent rapid signal decay during intravenous interface, with just 6.67 ± 3.91% baseline signal remaining after 1 day of implantation after normalization to the acute surgical baseline loss (Fig. 5d). In fact, we could barely discriminate individual SWV peaks after even a single day of implantation. Similarly, PEG-free npAu probes also showed indiscernible SWV peaks for baseline quantification after just 1 day (Supplementary Fig. 24). In contrast, SENSBIT retained 83.04 ± 11.92% of its baseline signal after 1 day of intravenous implantation and over 60% of its baseline signal after 7 days, extending sensor stability in blood from ≤12 h to at least 168 h (Fig. 5e and Supplementary Table 1).

To quantify sensitivity stability, we compared SWV signal gains after exposing our sensors to defined concentrations of kanamycin in PBS before and after intravenous implantation. After just 1 day of implantation, the pAu and npAu sensors exhibited indiscernible signal, but by manually extracting the SWV signals near the MB oxidation voltage (±0.15 V) before implantation, we determined that the pAu (Supplementary Fig. 25a) and npAu sensors (Supplementary Fig. 25b) exhibited severe deviation in their calibration curves

and greatly distorted sensitivity, such that the sensors could no longer faithfully report kanamycin concentrations. SENSBIT effectively overcame this issue, with near-identical calibration curves at days 0, 1, 4 and 7 post implantation (Fig. 5f). This unprecedented stability indicates that our SENSBIT design durably protects the sensor against fouling and degradation even after multiple days of continuous implantation and retains the capacity to accurately report analyte concentrations.

Finally, we evaluated SENSBIT's capacity to respond to changing concentrations of kanamycin before and after multiple days of implantation in free-moving rats. The biosensor probes were continuously measured in buffer (10 scans) with a sampling rate of ~3 min^{-1} and then subsequently challenged with 1 mM (5 scans), 0 mM (5 scans), 1 mM (5 scans), 2 mM (5 scans) and 0 mM (5 scans) kanamycin. As expected, the pAu (Supplementary Fig. 26a) and npAu sensors (Supplementary Fig. 26b) essentially lost their capacity to report kanamycin concentrations after just 1 day of intravenous interface. In striking contrast, SENSBIT retained real-time sensing capabilities with reproducible signal gains and comparable kinetics even after 7 days of implantation (Fig. 5g), with a ~3 min^{-1} reading frequency and a response profile that closely matched the readings collected pre-implantation on day 0. Importantly, the retracted SENSBIT consistently returned to baseline level in the absence of kanamycin, with minimal hysteresis. Thus, SENSBIT's week-long intravenous lifetime exceeds the clinical requirements of 4 days for peripheral intravenous (i.v.) device replacement.

Long-term intravenous pharmacokinetic monitoring in rats

We next demonstrated that SENSBIT is capable of intravenous real-time monitoring of kanamycin pharmacokinetics during anaesthesia after multiday implantation in free-moving rats. The implantable SENSBIT microwire probes bundled with Ag/AgCl reference electrode and Pt counter electrode were implanted in rat femoral veins, as depicted in Fig. 4a. After establishing baseline SWV readings, we disconnected the I/O port of the probe from the external potentiostat and surgically covered it with subcutaneous tissue, after which the wound was sutured before waking the rats. The rats were able to move freely while the probes were constantly subjected to blood flow and mechanical strain. After 1 day, we put the rats back under anaesthesia and re-exposed the I/O port of the probe for SWV analysis. The raw voltammograms after 25-h implantation maintained clear SWV peaks, while pAu control probes had indiscernible SWV peaks (Supplementary Fig. 27). We next characterized SENSBIT's capacity for intravenous monitoring of real-time changes in kanamycin pharmacokinetics after multiday continuous blood interface (Fig. 6). After 15–60 min of stable baseline visualization, we administered kanamycin via retro-orbital sinus injection (400 mg kg^{-1}), and observed corresponding SWV signal change with initial increase over the first 20–60 min followed by gradual decay due to elimination and metabolism. We generated calibration curves of the SENSBIT probe in vitro before and after 1, 2 or 4 days of continuous implantation and confirmed that there was minimal sensitivity drift or decay, with reproducible signal gain observed at each target concentration (Supplementary Fig. 28). Therefore, we were able to use the pre-implantation calibration curves for each SENSBIT probe to derive intravenously measured kanamycin concentrations with inverse-Langmuir standard curves in real time, without the need for correction or post

calibration. SENSBIT's operational stability thus enables long-term tracking of kanamycin pharmacokinetics from individual rats, even after 4 days of intravenous implantation (Supplementary Fig. 29).

Discussion

In summary, we have demonstrated a mucosa-inspired hierarchical sensor design that enables stable biochemical monitoring in complex biological matrices with robust performance after up to a month of exposure to biofluids. SENSBIT structurally mimics the intestinal mucosa nanoarchitecture with protruding bicontinuous nanoporous gold structures, hyperbranched PEG coating and electrochemically modified aptamer switches respectively emulating the microvilli, meshed glycocalyx coating and biological receptors of that natural system. This design enhances the sensor's functional stability during long-term exposure to undiluted serum or venous blood, creating a nanoscale physically restricted zone for molecular recognition while protecting against interferents. As a result, our SENSBIT retained >70% of its baseline signal and reproducible calibration curves after 1-month incubation in undiluted human serum in vitro, outperforming previously described electrochemical aptamer-based biosensors (Fig. 5e). When challenged after an extended period of intravenous implantation in free-moving rats, our sensor maintained >60% baseline signal and reproducible calibration curves, resulting in stable and consistent real-time sensing performance after a week's exposure to living tissue and continuously flowing blood. We also demonstrated that SENSBIT can faithfully track kanamycin pharmacokinetics of individual animals over the course of 4 days on the basis of pre-implantation calibration curves. Collectively, the results suggest that the simple multicomponent sensor design may serve as a general and robust platform for long-term monitoring of blood biomarkers, with durability and stability that exceeds those of previously reported sensors.

These results demonstrate a step towards achieving stable, accurate, continuous molecular detection directly in the bloodstream for extended periods of time. However, there are several important limitations to this study. First, this work has highlighted the capacity for continuously monitoring a small molecular target: the antibiotic kanamycin. We have also demonstrated the potential generalizability of our platform in experiments where we incorporated electrochemically modified aptamer switches that respond to DOX or ATP. Nevertheless, it will be important to more thoroughly validate the generalizability of the SENSBIT design with a range of other aptamers for additional targets of biomedical interest. This will in turn require not only interfacial structure tuning for mass transport in SENSBIT, but also the development of high-quality affinity reagents with target sensitivities in the appropriate physiological ranges and excellent specificity against interferents in blood[10,52]. Our current data suggest that SENSBIT is best suited for targets with molecular weight of <1 kDa, which will be an impediment to peptide and protein detection. Nevertheless, we believe that real-time monitoring of peptide and protein analytes is principally due to the inherent limitations imposed by binding and dissociation kinetics (Supplementary Note 5). As such, non-equilibrium interrogation strategies will probably be needed to track protein biomarkers at physiological concentrations[48]. Finally, for medical and clinical applications, it would be ideal if a wearable or implantable battery and wireless potentiostat could be

surgically connected to the SENSBIT, such as the electronics of pacemakers and deep brain stimulators. Despite the challenges ahead, SENSBIT offers a potential foundation for implantable sensors that could aid precision medicine and health monitoring.

Methods

Materials

All chemicals were purchased from Sigma-Aldrich, unless otherwise noted. Thiolated polyethylene glycol (PEG-SH), including linear methoxy PEG (mPEG-SH, M_W 2k, 10k, 20k), branched PEG (4-arm PEG-SH, M_W 10k; 8-arm PEG-SH, M_W 20k), was ordered from Creative PEGWorks. Fluorescent-labelled fibrinogen from human plasma, S1 nuclease and nuclease-free water (NFW) were purchased from Thermo Fisher. Human whole blood was ordered from the Stanford Blood Center. Pooled human plasma (blood-derived) and chicken plasma were purchased from Innovative Research. Kanamycin monosulfate (USP Grade) was purchased from Gold Biotechnology. Perfluoroalkoxy (PFA)-coated platinum wires (bare diameter 0.003”), PFA-coated tungsten wires (bare diameter 0.002”) and PFA-coated silver wires (bare diameter 0.008”) were purchased from A-M Systems. Gold wires (diameter 0.01”) and 10 k gold wire (diameter 0.01”) were purchased from Alfa Aesar and Amazon, respectively. Miniature heat-shrink tubes (pre-shrinking inner diameters 0.006” or 0.01”) were purchased from Nordson Medical and McMaster-Carr. The kanamycin aptamer was ordered from Integrated DNA Technologies, and the sequence used was /5ThioMC6-D/ GGGACT TGGTTTAGGTAATGAGTCCC/3MeBlN/, where 5ThioMC6-D indicates a thiol modification at the 5’ end and 3MeBlN indicates methylene blue labelling at the 3’ end. PBS buffer in this work was prepared by diluting 10× PBS and $MgCl_2$ with NFW to 1× PBS and 2 mM Mg^{2+}.

Planar gold and nanoporous gold preparation

A schematic of the device fabrication process is shown in Supplementary Fig. 1. For in vitro pAu sensors, a 90-nm-thick Au layer was patterned (1 mm × 1 mm for each working electrode) onto a pre-cleaned glass slide via shadow mask by electron beam evaporation (ATC-E, AJA International) after 10 nm Ti deposition. For in vitro SENSBIT sensors, nanoporous gold (npAu) film was patterned with shadow mask to produce 1 mm × 1 mm working electrodes (WE) on pre-cleaned glass slides with Ti/Au/Ag:Au (10/50/300 nm), as described in previous work[46]. The ratio of co-sputtered Ag:Au film was 2:1 (Lesker Sputter). Next, Ag was selectively etched by nitric acid (70% v/v) for 3 h, forming the npAu electrodes. For in vivo pAu microwire sensors, gold wires were cut into ~6-cm lengths and used as received. For in vivo SENSBIT microwire sensors, nanoporous gold wires were prepared by etching 10 k yellow gold wire in nitric acid (70% v/v) for 15 min. The prepared pAu and npAu electrodes were sequentially sonicated in acetone, 70% isopropyl alcohol and NFW for 2 min each. The cleaned pAu and npAu electrodes were stored in NFW before functionalization.

Microwire sensor preparation for in vivo applications

The pAu or npAu microwire WEs were insulated with heat-shrink tubes around the body of the wires, with ~2–5-mm length of electrode exposed for aptamer functionalization, as

described in our previous work[24]. The reference electrode (RE) was prepared by stripping a ~1-cm length of PFA insulation off the PFA-coated silver wires, followed by bleach oxidation of an 8-mm length of the exposed silver wire. The counter electrode (CE) was prepared by stripping a ~5-mm length of PFA insulation off the PFA-coated platinum electrode. The three electrodes were assembled and bundled with heat-shrink tubing as depicted in Fig. 4a and washed with 70% isopropyl alcohol and NFW. Heat-shrink tubes with lengths of 2–4 cm were used to strengthen the stem of the microwires for surgical manipulation.

pAu and SENSBIT sensor preparation and functionalization

Aptamer switches were suspended in NFW at a final concentration of 100 μM and stored at −20 °C before usage. To produce free thiol groups for aptamer immobilization, a 1,000-fold molar excess of freshly prepared Tris(2-carboxyethyl)phosphine hydrochloride (TCEP) solution was added to the aptamer switch solution and reacted for 40 min at room temperature in the dark. The mixture was then diluted to 1 μM aptamer in PBS. pAu and npAu electrodes were briefly dried with N_2 gas. For in vitro experiments, a polydimethylsiloxane (PDMS) chamber was prepared by punching a 6-mm-diameter hole in the 5-mm-thick PDMS film and subsequently putting the PDMS film onto the glass slide, such that the WEs were confined within the chamber. For in vivo experiments, the microwire electrodes or sensors were incubated in tubes. The samples were then immersed in the 1 μM aptamer solution for 1 h. After immobilization, pAu and npAu electrodes were washed twice with PBS. For the SENSBIT sensors, polymer coating was achieved by incubating the aptamer-immobilized npAu electrode with PEG solutions at room temperature for 3 h. PEG was prepared by dissolving in 70% isopropyl alcohol (1 % wt) with 65 °C heating and sonication. The pAu and npAu electrodes were then washed with excess PBS twice and incubated with ~10 mM MCH for 3 h at room temperature to fully passivate the remaining electrode surface. The pAu sensors and SENSBIT sensors were washed in excess PBS twice and then stored in PBS buffer at room temperature before electrochemical measurement.

Electrochemical characterizations of aptamer-based biosensors

Electrochemical measurements were conducted with PalmSens 4 potentiostat (PalmSens) and EmStat4 (PalmSens) with multiplexer (MUX8-R2 or MUX8, PalmSens). For in vitro experiments, the measurements were performed in PDMS wells. Commercial Ag/AgCl reference electrodes and Pt wire counter electrodes were used as received from CH Instruments. SWV was carried out in buffers or corresponding complex biological matrices over the potential range of ~−0.5 V to ~0.0 V with an amplitude of 20 mV, step size of 1 mV and pulse frequencies ranging from 20 to 200 Hz. To measure biosensor sensitivity in vitro, we obtained dose-response curves by subjecting the sensors to kanamycin concentrations ranging from 0.01–10 mM in various biological matrices by spiking in kanamycin stock solution (dilution <1% v/v) at room temperature. Data processing and visualization were performed with custom MATLAB code to automatically extract the SWV peak current levels (MATLAB R2023a). The calibration curves were generated by fitting the dose-response curves to the Langmuir isotherm model (Excel 365 and GraphPad Prism 10). Long-term incubation was achieved by loading 100–200 μl undiluted biofluids into the PDMS chamber, which was temporarily sealed with a PDMS lid before the next measurement. For

chronic measurements, biofluids were aliquoted from the same batch of biological matrix and thawed 2 h before the measurement followed by gentle mixing.

For in vivo intravenous measurement, bundled WE, RE and CE were connected to the multiplexer with a customized adaptor that minimizes the strain of the microwire electrodes. SWV was carried out after implantation over the potential range of ~−0.5 V to ~0.0 V with an amplitude of 20 mV, step size of 1 mV and pulse frequencies ranging from 20 to 100 Hz, adjusted according to the signal levels and signal noise. Real-time data processing and visualization were performed with custom MATLAB code to automatically extract the SWV peak current levels, as described in our previous work[24]. For sensor calibration measurements before and after in vivo implantation, pAu or SENSBIT sensors were connected to the multiplexer with the customized adaptor and measured in a tube. To calibrate the biosensor sensitivity, we obtained the dose-response curve by sequentially adding kanamycin stock solution to the buffer, followed by ~10 times pipette mixing. For real-time measurements before and after in vivo implantation, pAu or SENSBIT sensors were continuously measured at a sampling rate of ~3 min^{-1}. Kanamycin concentration changes were achieved by dipping the sensors into kanamycin solution of different concentrations.

SENSBIT optimization via nuclease-aided screening platform

Biosensors with immobilized aptamers and various surface conditions were prepared on glass slides and incubated in 200 μl S1 nuclease buffer with 1 mM Zn^{2+} (Thermo Fisher) before electrochemical characterization. During screening, the biosensors were continuously measured with SWV scanning at a sampling rate of 0.5 min^{-1}. After stabilizing for ~30 min in S1 nuclease buffer under continuous electrochemical characterization, S1 nuclease was added to the biosensor buffer to reach a final nuclease concentration of 60 U ml^{-1}. The continuous electrochemical signals were tracked and analysed with custom MATLAB code to automatically extract the SWV peak current levels.

Whole-blood adhesion assay

Human whole blood was freshly prepared by the Stanford Blood Center. The blood product orders did not include special instructions regarding donor age, gender, ethnicity or other information. Sex and gender were not considered in this study. The blood was used as prepared at room temperature. After gentle mixing of the fresh blood, ~100 μl human whole blood was added to in vitro sensors within the PDMS chamber and incubated at room temperature in the dark with a sealing PDMS lid. For electron microscopy characterization, we then added 20 μl 1 M $CaCl_2$ to the PDMS chamber and incubated it for 10 min, followed by a gentle PBS wash via pipette. After removing the PDMS chambers, the samples were immersed in fixation solution (4% paraformaldehyde, 0.4% glutaraldehyde in 0.2 M sodium cacodylate) at room temperature for 10 min. After three washes with NFW, the samples were immersed in 1% OsO_4 staining solution for 1 h in the dark. After three washes with NFW, the samples were transferred to a series of ethanol baths: 30%, 50%, 70%, 80%, 90%, 96% and absolute (each 10 min). The fixed samples were transferred to a critical point dryer (Tousimis 815, Series A) and dried. Finally, the samples were mounted and sputter coated with a thin layer of Au/Pd (Denton Desk II Sputter Coater). After imaging,

pseudocolour was applied to provide contrast of blood cell adhesion on samples. According to the visually distinguishable cells, blood cell coverage was identified within four randomly selected regions and extracted by bandpass filtering, thresholding and binarizing with Fiji ImageJ 1.53t (four areas per sample were obtained), followed by MATLAB analysis. For the fibrinogen assay, fluorescently labelled fibrinogen (150 μg ml^{-1}) was added to the blood, which was then incubated in the sensor sample chamber for 2 h at 37 °C. After washing with PBS, the samples were imaged with a Leica DM4 upright epifluorescence microscope. Quantification was performed by thresholding the fluorescent features, followed by binarization and ratio calculation with MATLAB. The threshold was manually set to 800 for all images, and the area covered by fibrin was extracted from the measurements (four areas per sample were obtained).

Surface and tomography characterization by SEM and FIB-SEM

Sensor surface characterization was carried out by SEM (Thermo Fisher, Apreo S LoVac and FEI Magellan 400 XHR). The samples underwent plasma cleaning within the SEM chamber and were imaged with 2–5 keV. Tomography characterization was carried out using a FIB-SEM (FEI Helios NanoLab 600i DualBeam), which combines high-resolution SEM imaging and FIB milling. To characterize the cross-section of the nanoporous gold structure in Fig. 1b, a thin layer (~300 nm) of Pt was deposited on the field of interest before FIB milling. For cell or protein adhesion characterization, no Pt was deposited within the SEM chamber to preserve the intact interface between sensor and biological materials. To expose the sensor interface, fouling components on the electrode surface were first located in top-view SEM, after which FIB was used in situ to carry out vertical dissection at the desired locations. The dissection cross-sections were visualized through SEM via 52° tilting. The analysis began with a large field of view examination, followed by focused assessments of at least four randomized specific regions.

Live animal studies

Live animal studies were performed with male Sprague–Dawley rats under Stanford Laboratory Animal Care (APLAC) protocol number 33226. All rats used in this work were purchased from Charles River Laboratories, with a weight range of 200–450 g and an age range of 1–4 months. The rats were anaesthetized using isoflurane gas (2.5%) during implantation procedures and monitored continuously. The femoral veins of the rats were isolated and exposed with a small incision, through which the microwire probes were implanted and pushed far into the vein. The microwire probes were secured in place while maintaining the intravenous blood flow, after which the incision was closed and sutured with sutures and a small amount of tissue glue to anchor the suture wire. For the in vivo pharmacokinetic monitoring experiments, the probes were connected to the external potentiostat, and continuous SWV scanning was performed under anaesthesia. Kanamycin (100 mM) was administered via retro-orbital sinus injection to reach 400 mg kg^{-1} dosage. For multiday sensor implantation in free-moving rats, the microwire probes were sterilized with a UV light sanitizer (Amazon) before implantation. The implantation wounds were sutured and secured with wound clips (Fine Science Tools). The animals were monitored daily for post-surgery recovery and maintained for up to 7 days. At the end of the experiments, animals were anaesthetized using isoflurane gas and the microwire probes were

retracted for post-implantation analysis. Rats were then euthanized by exsanguination while under general anaesthesia.

Statistics and reproducibility

All experiments were repeated at least three times. Data are shown as mean ± s.d. ($n \geq 3$) and were analysed with GraphPad Prism 10 software. Differences are considered statistically significant at $P < 0.05$.

Supplementary Material

Refer to Web version on PubMed Central for supplementary material.

Acknowledgements

This work was supported by the Helmsley Trust, Wellcome LEAP SAVE programme, Stanford Material and Child Health Research Institute pilot grant and the National Institutes of Health (NIH, OT2OD025342). Part of this work was performed at the Stanford Nano Shared Facilities (SNSF), Stanford Nanofabrication Facility (SNF) and Stanford University Cell Sciences Imaging Core Facility (RRID:SCR_017787), supported by the National Science Foundation under award ECCS-2026822 and ECCS-1542152. We thank the Canary Center at Stanford for Cancer Early Detection for providing facilities and the Stanford Veterinary Service Center for their assistance with animal care and training. Viability and cell proliferation assays were performed by N. Quispe Calla at Stanford Transgenic, Knockout and Tumor Model Center. Flow cytometry analysis for this project was done on instruments in the Stanford Shared FACS Facility. Y.C. was supported by the T. S. Lo Graduate Fellowship at Stanford University. Z.O. was supported by the Wu Tsai Neurosciences Institute at Stanford University. Y.C. also thanks E. Sullivan of the Technical Communications Program at Stanford for thoughtful feedback on writing, and E. Bagley and N. Torres for lab management support.

Data availability

The main data supporting the findings of this study are available within the paper and its supplementary information files. Extra data are available from the corresponding author upon request. Source data for Figs. 1–6 are provided with this paper.

References

1. Sohn E Diagnosis: frontiers in blood testing. Nature 549, S16–S18 (2017). [PubMed: 28953862]
2. Gao W et al. Fully integrated wearable sensor arrays for multiplexed in situ perspiration analysis. Nature 529, 509–514 (2016). [PubMed: 26819044]
3. Kim J, Campbell AS, de Ávila BE-F & Wang J Wearable biosensors for healthcare monitoring. Nat. Biotechnol. 37, 389–406 (2019). [PubMed: 30804534]
4. Ye C et al. A wearable aptamer nanobiosensor for non-invasive female hormone monitoring. Nat. Nanotechnol. 19, 330–337 (2024). [PubMed: 37770648]
5. Sempionatto JR et al. An epidermal patch for the simultaneous monitoring of haemodynamic and metabolic biomarkers. Nat. Biomed. Eng. 5, 737–748 (2021). [PubMed: 33589782]
6. Wang M et al. A wearable electrochemical biosensor for the monitoring of metabolites and nutrients. Nat. Biomed. Eng. 6, 1225–1235 (2022). [PubMed: 35970928]
7. Tavallaie R et al. Nucleic acid hybridization on an electrically reconfigurable network of gold-coated magnetic nanoparticles enables microRNA detection in blood. Nat. Nanotechnol. 13, 1066–1071 (2018). [PubMed: 30150634]
8. Drummond TG, Hill MG & Barton JK Electrochemical DNA sensors. Nat. Biotechnol. 21, 1192–1199 (2003). [PubMed: 14520405]
9. Nakatsuka N et al. Aptamer–field-effect transistors overcome Debye length limitations for small-molecule sensing. Science 362, 319–324 (2018). [PubMed: 30190311]

10. Flynn CD et al. Biomolecular sensors for advanced physiological monitoring. Nat. Rev. Bioeng. 1, 560–575 (2023).
11. Wang L et al. Rapid and ultrasensitive electromechanical detection of ions, biomolecules and SARS-CoV-2 RNA in unamplified samples. Nat. Biomed. Eng. 6, 276–285 (2022). [PubMed: 35132229]
12. Yin F et al. DNA-framework-based multidimensional molecular classifiers for cancer diagnosis. Nat. Nanotechnol. 18, 677–686 (2023). [PubMed: 36973399]
13. Swensen JS et al. Continuous, real-time monitoring of cocaine in undiluted blood serum via a microfluidic, electrochemical aptamer-based sensor. J. Am. Chem. Soc. 131, 4262–4266 (2009). [PubMed: 19271708]
14. Vallée-Bélisle A, Ricci F & Plaxco KW Thermodynamic basis for the optimization of binding-induced biomolecular switches and structure-switching biosensors. Proc. Natl Acad. Sci. USA 106, 13802–13807 (2009). [PubMed: 19666496]
15. Ferguson BS et al. Real-time, aptamer-based tracking of circulating therapeutic agents in living animals. Sci. Transl. Med. 5, 213ra165 (2013).
16. Arroyo-Currás N et al. Real-time measurement of small molecules directly in awake, ambulatory animals. Proc. Natl Acad. Sci. USA 114, 645–650 (2017). [PubMed: 28069939]
17. Parolo C et al. Real-time monitoring of a protein biomarker. ACS Sens. 5, 1877–1881 (2020). [PubMed: 32619092]
18. Sabaté del Río J, Henry OYF, Jolly P & Ingber DE An antifouling coating that enables affinity-based electrochemical biosensing in complex biological fluids. Nat. Nanotechnol. 14, 1143–1149 (2019). [PubMed: 31712665]
19. Song E, Li J, Won SM, Bai W & Rogers JA Materials for flexible bioelectronic systems as chronic neural interfaces. Nat. Mater. 19, 590–603 (2020). [PubMed: 32461684]
20. Shaver A & Arroyo-Currás N The challenge of long-term stability for nucleic acid-based electrochemical sensors. Curr. Opin. Electrochem. 32, 100902 (2022). [PubMed: 36092288]
21. Leslie DC et al. A bioinspired omniphobic surface coating on medical devices prevents thrombosis and biofouling. Nat. Biotechnol. 32, 1134–1140 (2014). [PubMed: 25306244]
22. Jaffer IH & Weitz JI The blood compatibility challenge. Part 1: blood-contacting medical devices: the scope of the problem. Acta Biomater. 94, 2–10 (2019). [PubMed: 31226480]
23. Frutiger A et al. Nonspecific binding—fundamental concepts and consequences for biosensing applications. Chem. Rev. 121, 8095–8160 (2021). [PubMed: 34105942]
24. Chan D et al. Combinatorial polyacrylamide hydrogels for preventing biofouling on implantable biosensors. Adv. Mater. 34, 2109764 (2022).
25. Li S et al. Implantable hydrogel-protective DNA aptamer-based sensor supports accurate, continuous electrochemical analysis of drugs at multiple sites in living rats. ACS Nano 17, 18525–18538 (2023). [PubMed: 37703911]
26. Li H et al. A biomimetic phosphatidylcholine-terminated monolayer greatly improves the in vivo performance of electrochemical aptamer-based sensors. Angew. Chem. Int. Ed. 56, 7492–7495 (2017).
27. Watkins Z, Karajic A, Young T, White R & Heikenfeld J Week-long operation of electrochemical aptamer sensors: new insights into self-assembled monolayer degradation mechanisms and solutions for stability in serum at body temperature. ACS Sens. 8, 1119–1131 (2023). [PubMed: 36884003]
28. Daggumati P, Matharu Z, Wang L & Seker E Biofouling-resilient nanoporous gold electrodes for DNA sensing. Anal. Chem. 87, 8618–8622 (2015). [PubMed: 26274576]
29. Seo JW et al. Real-time monitoring of drug pharmacokinetics within tumor tissue in live animals. Sci. Adv. 8, eabk2901 (2022). [PubMed: 34995112]
30. Peterson LW & Artis D Intestinal epithelial cells: regulators of barrier function and immune homeostasis. Nat. Rev. Immunol. 14, 141–153 (2014). [PubMed: 24566914]
31. Wagner CE, Wheeler KM & Ribbeck K Mucins and their role in shaping the functions of mucus barriers. Annu. Rev. Cell Dev. Biol. 34, 189–215 (2018). [PubMed: 30296390]
32. Luo L Principles of Neurobiology (Garland Science, 2020).

33. Latz E et al. Ligand-induced conformational changes allosterically activate Toll-like receptor 9. Nat. Immunol. 8, 772–779 (2007). [PubMed: 17572678]
34. Bansil R & Turner BS The biology of mucus: composition, synthesis and organization. Adv. Drug Deliv. Rev. 124, 3–15 (2018). [PubMed: 28970050]
35. Sun WW et al. Nanoarchitecture and dynamics of the mouse enteric glycocalyx examined by freeze-etching electron tomography and intravital microscopy. Commun. Biol. 3, 5 (2020). [PubMed: 31925335]
36. Shaver A, Curtis SD & Arroyo-Currás N Alkanethiol monolayer end groups affect the long-term operational stability and signaling of electrochemical, aptamer-based sensors in biological fluids. ACS Appl. Mater. Interfaces 12, 11214–11223 (2020). [PubMed: 32040915]
37. Companion Handbook to the WHO Guidelines for the Programmatic Management of Drug-resistant Tuberculosis (World Health Organization, 2014).
38. Chien JC, Baker SW, Soh HT & Arbabian A Design and analysis of a sample-and-hold CMOS electrochemical sensor for aptamer-based therapeutic drug monitoring. IEEE J. Solid State Circuits 55, 2914–2929 (2020). [PubMed: 33343021]
39. Lowe S, O'Brien-Simpson NM & Connal LA Antibiofouling polymer interfaces: poly(ethylene glycol) and other promising candidates. Polym. Chem. 6, 198–212 (2015).
40. Sharma S, Johnson RW & Desai TA XPS and AFM analysis of antifouling PEG interfaces for microfabricated silicon biosensors. Biosens. Bioelectron. 20, 227–239 (2004). [PubMed: 15308226]
41. Shaver A et al. Nuclease hydrolysis does not drive the rapid signaling decay of DNA aptamer-based electrochemical sensors in biological fluids. Langmuir 37, 5213–5221 (2021). [PubMed: 33876937]
42. Chandrasekaran AR Nuclease resistance of DNA nanostructures. Nat. Rev. Chem. 5, 225–239 (2021).
43. Armstrong JK, Wenby RB, Meiselman HJ & Fisher TC The hydrodynamic radii of macromolecules and their effect on red blood cell aggregation. Biophys. J. 87, 4259–4270 (2004). [PubMed: 15361408]
44. Lin P-H & Li B-R Antifouling strategies in advanced electrochemical sensors and biosensors. Analyst 145, 1110–1120 (2020). [PubMed: 31916551]
45. Laktionov MY, Zhulina EB, Richter RP & Borisov OV Polymer brush in a nanopore: effects of solvent strength and macromolecular architecture studied by self-consistent field and scaling theory. Polymers 13, 3929 (2021). [PubMed: 34833228]
46. Fu K et al. Accelerated electron transfer in nanostructured electrodes improves the sensitivity of electrochemical biosensors. Adv. Sci. 8, 2102495 (2021).
47. White RJ, Rowe AA & Plaxco KW Re-engineering aptamers to support reagentless, self-reporting electrochemical sensors. Analyst 135, 589–594 (2010). [PubMed: 20174715]
48. Maganzini N, Thompson I, Wilson B & Soh HT Pre-equilibrium biosensors as an approach towards rapid and continuous molecular measurements. Nat. Commun. 13, 7072 (2022). [PubMed: 36400792]
49. Jaffer IH, Fredenburgh JC, Hirsh J & Weitz JI Medical device-induced thrombosis: what causes it and how can we prevent it? J. Thromb. Haemost. 13, S72–S81 (2015). [PubMed: 26149053]
50. Weber M et al. Blood-contacting biomaterials: in vitro evaluation of the hemocompatibility. Front. Bioeng. Biotechnol. 6, 99 (2018). [PubMed: 30062094]
51. Bard AJ, Faulkner LR & White HS Electrochemical Methods: Fundamentals and Applications (John Wiley & Sons, 2022).
52. Das J et al. Reagentless biomolecular analysis using a molecular pendulum. Nat. Chem. 13, 428–434 (2021). [PubMed: 33686229]

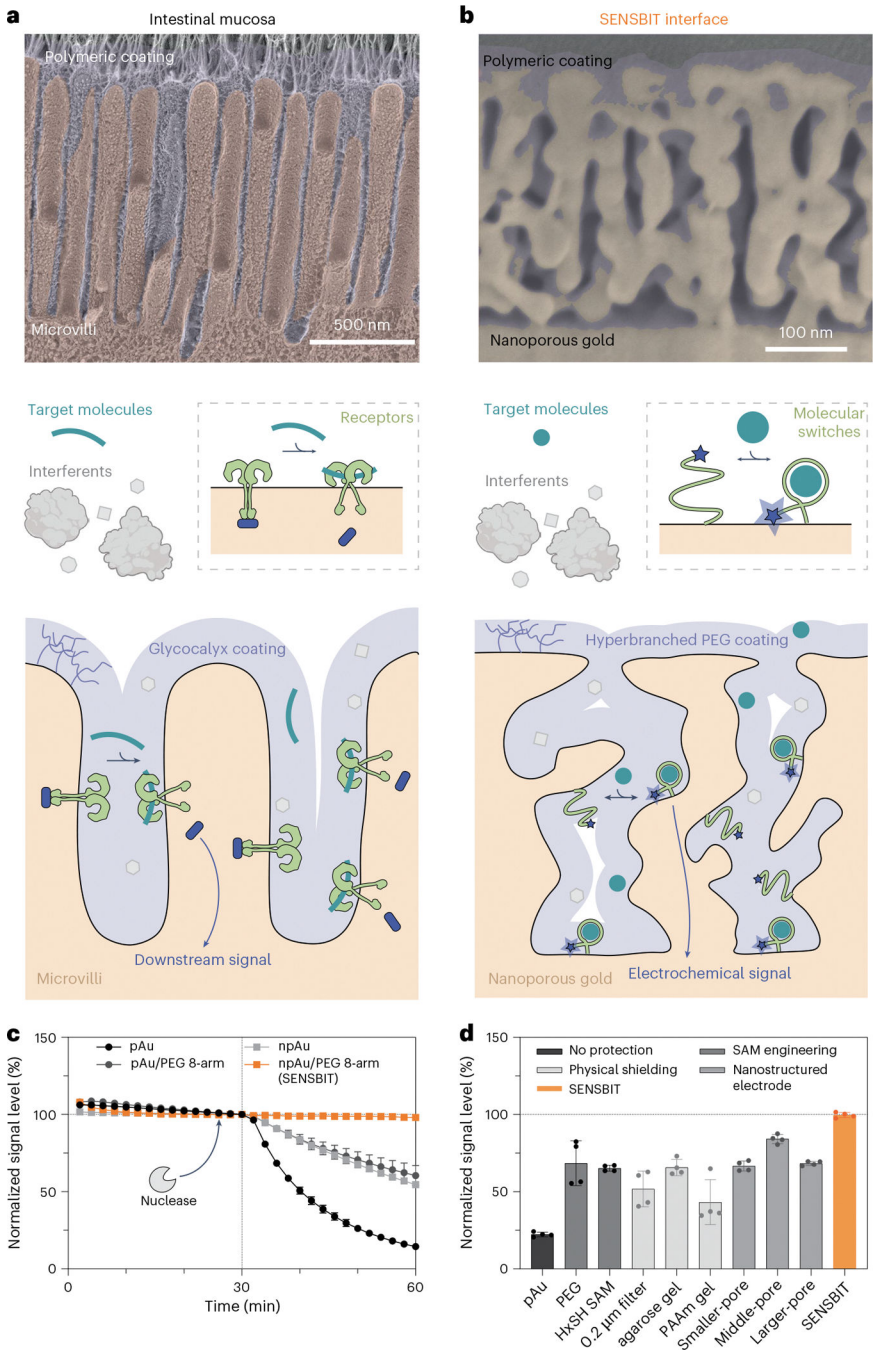

Fig. 1 |. A biologically inspired approach for long-term, stable electrochemical sensing in complex biological matrices.

a, Top: an electron microscopy cross-section of the intestinal mucosa, which is covered in epithelial microvilli that are adorned with a polymeric glycocalyx coating and pattern-recognition receptors. Bottom: diagram depicting components in simplified form. This system insulates the epithelium from direct contact with gut bacteria while still allowing bacteria-derived biochemical signals to access relevant receptors. The electron microscopy image was adapted and coloured with permission from ref. 35 under Creative Commons

Attribution 4.0 International License. **b**, SENSBIT emulates this structure with a nanoporous gold layer, a protective polymeric coating and aptamer switch-based receptors for detecting relevant small-molecule analytes. Top: an electron microscopy cross-section of the sensor interface after cutting with a focused Ga^+ ion beam. Bottom: a simplified diagram of the SENSBIT system. Created with BioRender.com. **c**, We tested resistance to protein interference by monitoring real-time electrochemical signal decay for aptamer-modified planar gold (pAu) and nanoporous gold (npAu) electrodes with or without hyperbranched (M_W = 20 kDa) PEG before and after spiking in S1 nuclease. We performed a 30-min baseline measurement before spiking in 60 U ml^{-1} S1 nuclease. **d**, Protein resistance comparison among existing sensor protection strategies and SENSBIT. We modified aptamer-immobilized sensors with different reported protection methods: SAM engineering (PEG coating and 1-hexanethiol passivation[36]); physical shielding (microporous polysulfone membrane attachment[16], agarose hydrogel coating[25] and PAAm hydrogel coating[24]); or nanostructured electrodes with different pore sizes[29]. The plot shows electrochemical signals remaining after 30 min exposure to 60 U ml^{-1} S1 nuclease. Real-time electrochemical signal decay and statistical analysis with calculated *P* values are shown in Supplementary Fig. 7. All datapoints and error bars represent mean ± s.d. of 4 sensor replicates.

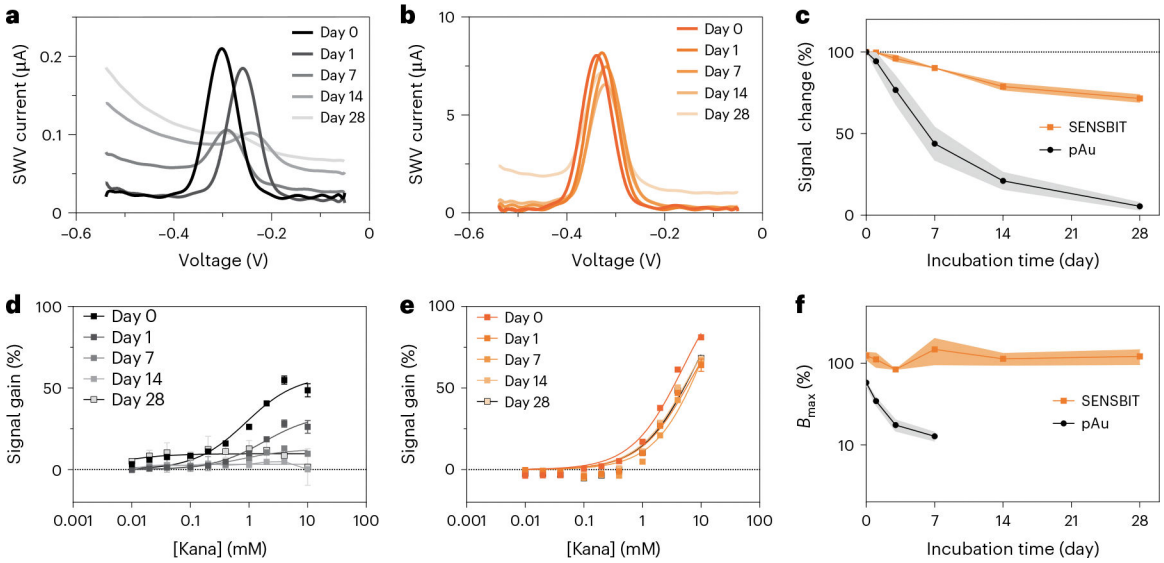

Fig. 2 |. SENSBIT performance after a month-long incubation in human serum in vitro.

a,**b**, SWV signal drift after exposing (**a**) a PEG-free pAu (MCH-only) electrode or (**b**) the SENSBIT electrode to undiluted human serum for a month. SWV frequency = 200 Hz, amplitude = 20 mV. **c**, Stability of baseline electrochemical signal over the course of a month-long incubation in human serum for SENSBIT versus the pAu sensor. The shaded area indicates the error bars of sensor signal changes (mean ± s.d., $n = 4$ sensors). **d**,**e**, Calibration curves obtained at multiple timepoints during a month-long incubation in undiluted human serum for (**d**) pAu and (**e**) SENSBIT (mean ± s.d., $n = 4$ sensors). **f**, Drift from fitted maximum signal gain of the sensor, B_{max} ($R^2 > 0.80$), over the course of a month-long incubation in human serum for SENSBIT versus the pAu sensor. The dots represent the best-fit values for B_{max} and the shaded area indicates the 95% confidence intervals of B_{max} obtained through Langmuir isotherm model fitting (hyperbola) in Prism ($n = 4$ sensors).

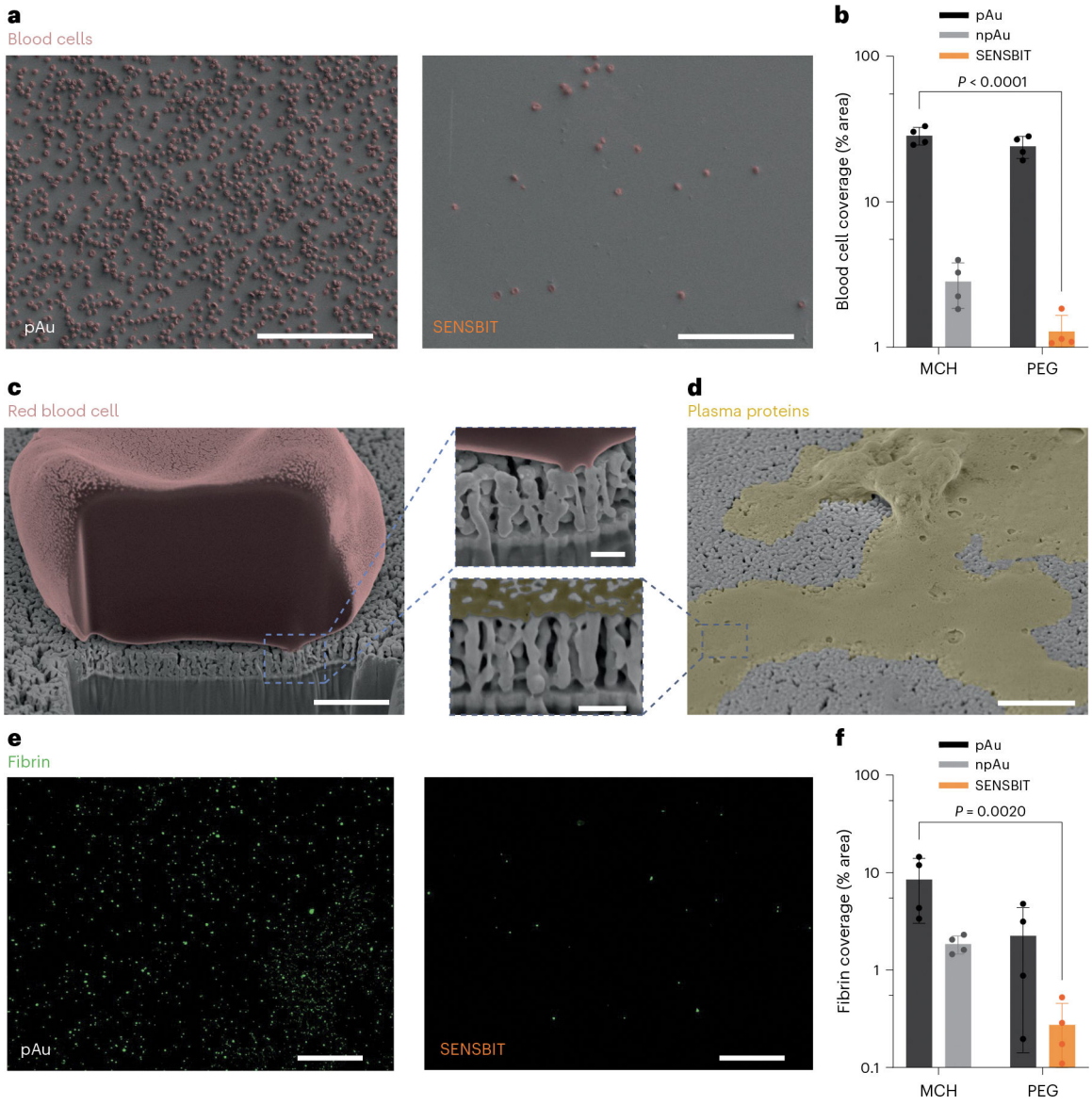

Fig. 3 |. SENSBIT exhibits greatly reduced surface contamination in human whole blood.
a, Top-view SEM images of pAu (left) and SENSBIT (right) sensor electrodes after 14 h incubation with fresh human blood. Scale bars, 100 μm. **b**, Extent of blood cell fouling for PEG-free and PEG-coated pAu and npAu sensors (mean ± s.d., $n = 4$ regions of interest (ROIs)). **c**, In situ FIB-SEM cross-section image of a blood cell attached to SENSBIT. Scale bar, 1 μm. Magnification shows that direct interactions between SENSBIT and the cell membrane are limited to a small area, leaving most of the sensor's biochemical interface intact. Scale bar, 200 nm. **d**, SEM image of SENSBIT electrodes after incubation for 19 days in 0.2-μm-filtered chicken plasma. Scale bar, 1 μm. Magnification shows a FIB-SEM cross-section revealing how the internal pore system remains unfouled even beneath apical surfaces exhibiting protein fouling. Scale bar, 200 nm. **e**, Fluorescence micrographs of sensor electrodes after 2 h incubation with fresh human blood containing fluorescently labelled fibrinogen (150 μg ml^{-1}) show considerably more fibrin adhesion on the pAu

electrode (left) versus SENSBIT (right). Scale bar, 100 μm. **f**, Fluorescently labelled fibrin coverage for PEG-free and PEG-coated pAu and npAu electrodes (mean ± s.d., $n = 4$ ROIs). Fluorescence is plotted on a logarithmic intensity scale. The P values between conventional PEG-free pAu electrodes and SENSBITs were calculated using the two-way analysis of variance (ANOVA) model in Prism.

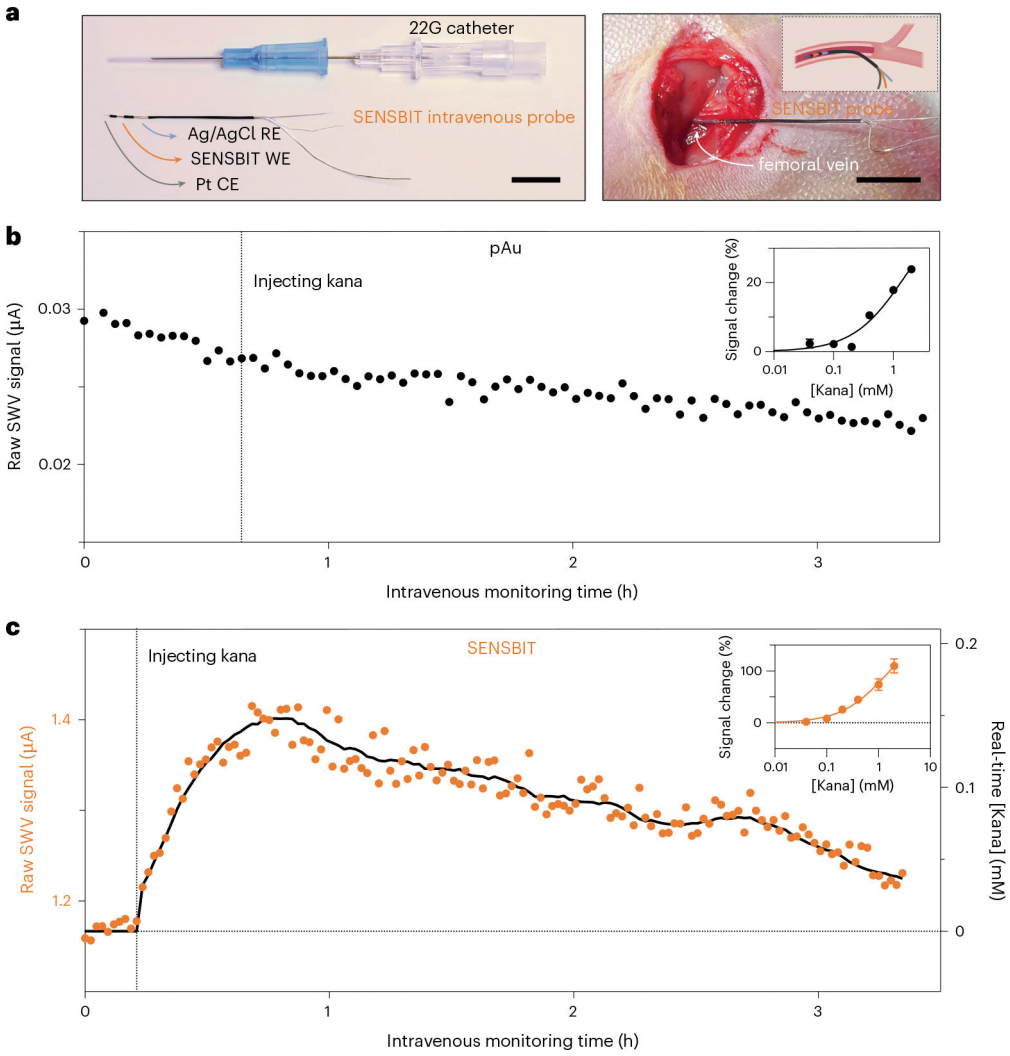

Fig. 4 |. In vivo real-time kanamycin monitoring over several hours with SENSBIT.

a, Left: the SENSBIT intravenous biosensor probe compared to a 22G clinical IV catheter. Scale bar, 10 mm. Right: the surgical condition where the SENSBIT probe was implanted within the femoral vein to achieve a direct interface with the blood in anaesthetized rats. Inset: schematic of SENSBIT implanted in the femoral vein. **b**,**c**, Real-time SWV scanning with an intravenously implanted (**b**) pAu sensor or (**c**) SENSBIT sensor over several hours after the injection of a single bolus of drug (time marked with dotted line). Insets: sensor calibration curves in buffer before implantation (mean ± s.d., 3 measurements per concentration). Individual pharmacokinetic data from two other rats are shown in Supplementary Fig. 18.

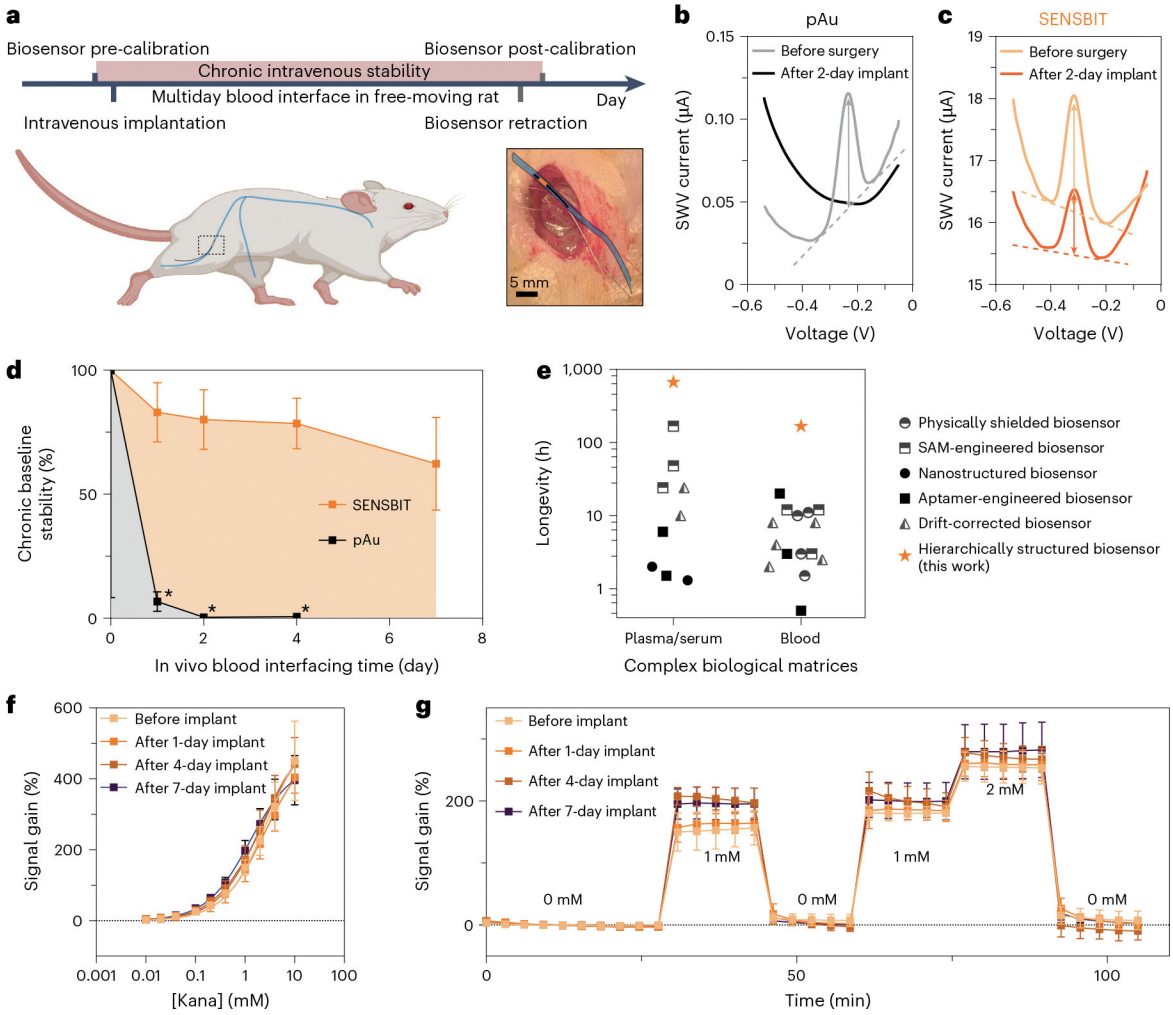

Fig. 5 |. Impact of week-long sensor–blood interface in free-moving rats.

a, Workflow for our evaluation of long-term SENSBIT implantation in free-moving rats. Sensors were surgically implanted within rat femoral veins for multiple days before being extracted for further evaluation. Scale bar, 5 mm. Created with BioRender.com. **b**,**c**, Raw SWV baseline signal degradation in kanamycin-free buffer after 2 days of continuous implantation of (**b**) pAu or (**c**) SENSBIT electrodes. **d**, Baseline electrochemical signals of the two sensors after multiday implantation. The data were normalized to signal loss after surgery (Supplementary Fig. 23). An * indicates that SWV peaks were inadequately resolved for quantitative data analysis. **e**, Comparison of device longevity of previously published electrochemical aptamer-based sensors exposed to blood derivatives and whole blood. Shapes and patterns of the symbols distinguish these various strategies. References are provided in Supplementary Table 1. **f**, Calibration curves of SENSBIT before and after 1, 4 or 7 days of intravenous implantation. **g**, Continuous kanamycin monitoring with SENSBIT before and after 1-, 4- or 7-day implantation in femoral veins of free-moving rats. Data points and error bars represent mean ± s.d. of 3 independent replicates, with different sensors in different animal femoral veins.

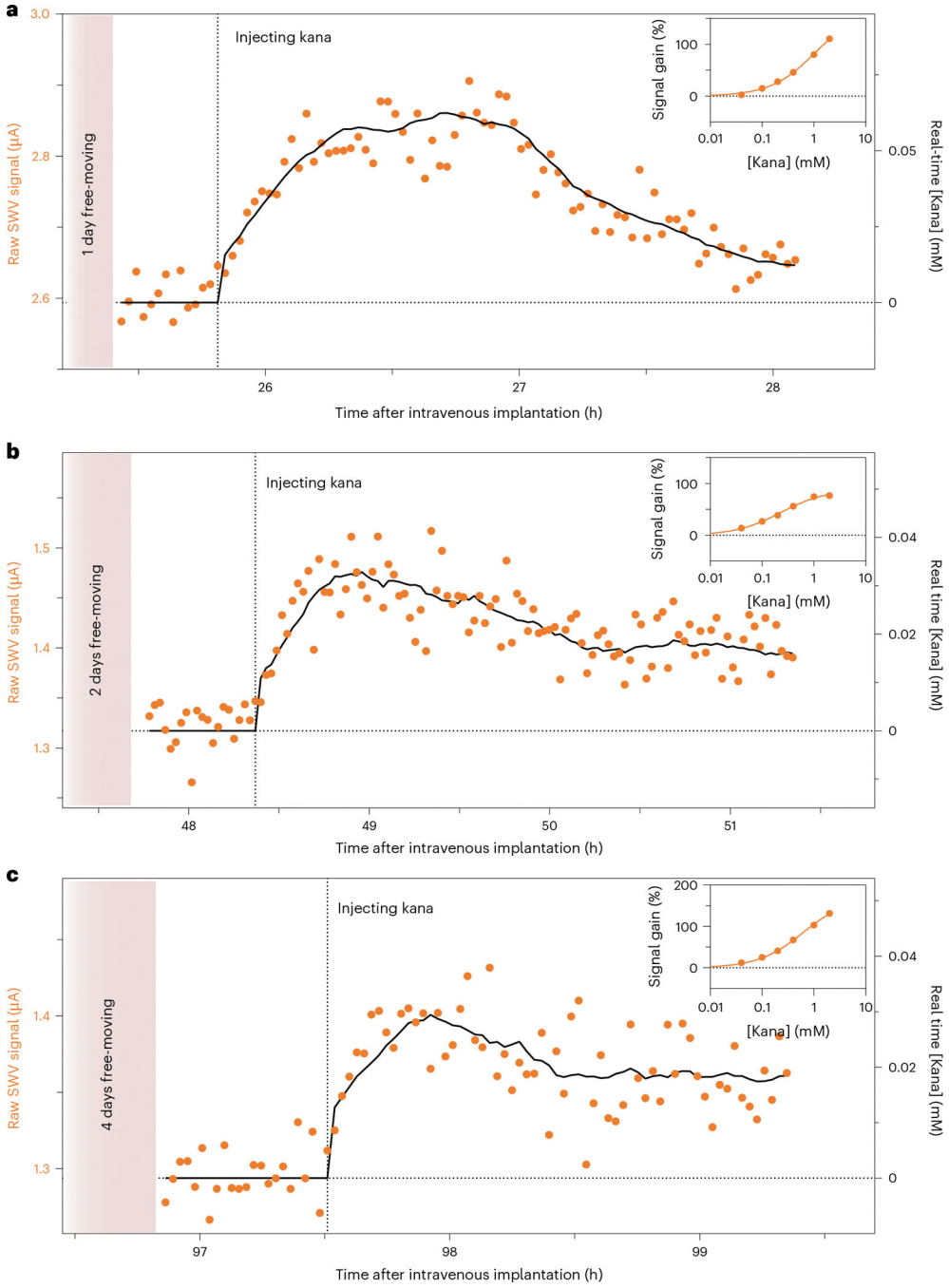

Fig. 6 |. Intravenous real-time monitoring of kanamycin pharmacokinetics during anaesthesia with SENSBIT after 1, 2 or 4 days of i.v. implantation in free-moving rats.

a–**c**, Real-time SWV readings with SENSBIT sensors from three different rats (**a**) 1, (**b**) 2 or (**c**) 4 days after i.v. implantation. Readings were collected over several hours after the injection of a single bolus of drug (400 mg kg^{-1}, injection time marked with vertical dotted line). Insets: sensor calibration curves in buffer before implantation (mean ± s.d., 3 measurements per concentration).